Journal of the Iranian Chemical Society (2022) 19:4503–4513
https://doi.org/10.1007/s13738-022-02618-4

ORIGINAL PAPER

Herbal synthesis of integrated binary-semiconductor nanocomposites of silver doped CuO with ZnO/SnO_2 for antibacterial activities and photocatalytic degradation of organic dyes

Avis Tresa Babu[1] · **Rosy Antony**[2]

Received: 17 October 2021 / Accepted: 24 June 2022 / Published online: 6 August 2022

Abstract

Sida rhombifolia leaf extract was used to synthesize heterostructured nanocomposites Ag@CuO/ZnO and Ag@CuO/SnO_2 by sol–gel combustion method followed by calcination. Through this ecofriendly approach, we could minimize the utilization of toxic chemicals as the bioactive components present in the plant extract act as capping and complexing agents. XRD studies indicated the formation of various crystalline phases of the congeners of the heterostructured nanocomposites. FESEM studies revealed irregular aggregates for AZC of particle size between 100 and 500 nm whereas uniformly arranged distorted spheres for ASC. The UV-DRS spectra helped to assess the reduced band gap energy from tau plot. The PL emission peaks of ZnO and SnO_2 point towards the crystal defects in their lattices. The as-prepared ternary nanocomposites have resistivity to the growth of *Escherichia coli, Klebsiella pneumoniae, Pseudomonas aeroginosa, Streptococcus mutans and Staphylococcus aureus* with greater inhibition zones which showed their superior antibacterial activity. They are proved to be excellent photocatalysts for the degradation of hazardous organic dyes into harmless products and reduction of aromatic compounds into useful chemicals. Thus, the facile, low-cost and environmentally sustainable green synthesis provides Ag@CuO/ZnO and Ag@CuO/SnO_2 nanocomposites with multifunctional efficacy.

Graphical abstract

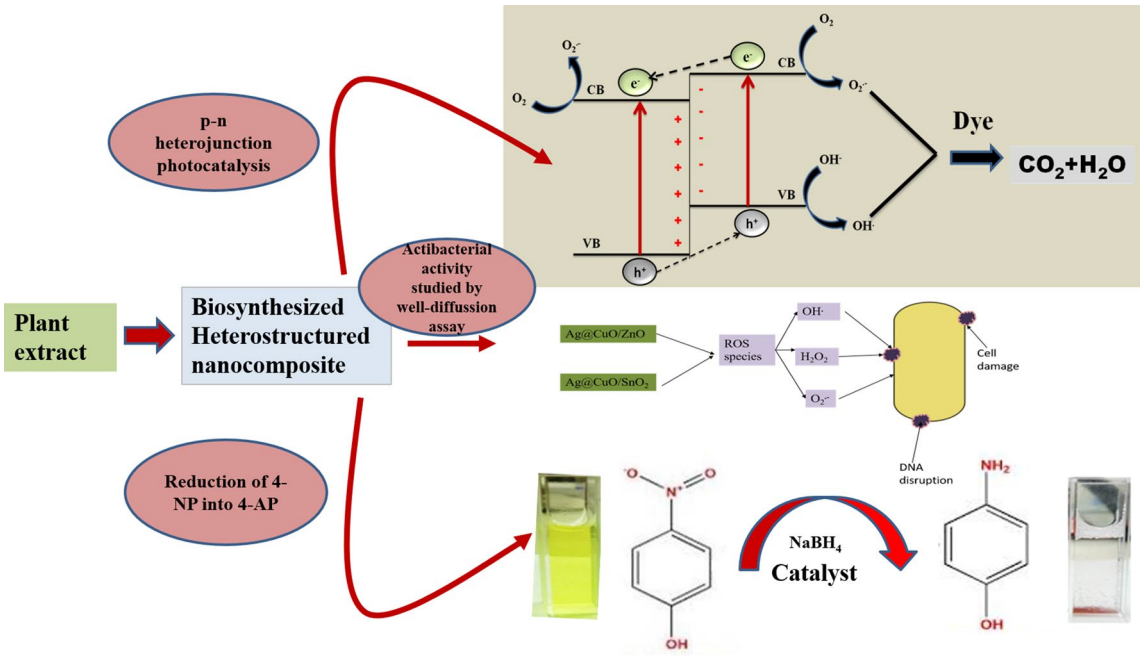

Extended author information available on the last page of the article

Keywords Binary-semiconductor nanocomposites · p-n heterojunction · *Sida rhombifolia* · Antibacterial agent · Photocatalysis · Catalytic reduction

Introduction

Synthetic dyes and aromatic compounds present in industrial effluents are harmful to living beings and cause severe environmental issues. Waste water treatment techniques include adsorption, photodegradation, filtration, reverse osmosis, coagulation, etc. Photocatalysis is an environmentally viable green technology since it utilizes sunlight as the energy source for degradation of toxic industrial wastes into harmless products. The multifunctional nanocomposites find wide applications in energy conversion, pollution control and modification of photoelectrochemical processes [1–4]. They can be prepared by co-precipitation, sol–gel technique, hydrothermal method, etc. The preparation of photocatalysts by green method has emerged as an environmentally benign and economically viable route to prepare metal oxide nanocomposites in a simple way. Toxic organic solvents, capping agents or stabilizers are not used. This is also advantageous in the sense that the synthetic procedure can be scaled up since the plant materials are abundant in the locality. Green synthesis of photocatalysis with ZnO or CuO etc. yield nanocomposites with moderate degradation efficiency whereas the synthesis of integrated nano metal oxides with p–n junction results in high efficacy.

The n-type (SnO_2, ZnO, TiO_2, In_2O_3, WO_3) and p-type (Cr_2O_3, Co_3O_4, CuO, Ag_2O, CdO) semiconductor metal oxides can be combined to make use of the effects of the heterojunction and improve photocatalytic efficiency. Heterostructured nanocomposites contain coupled semiconductors with metals of suitable band gap energies. Compared to individual components, the photocatalytic efficiency has been found to increase synergistically for coupled metal oxides by the suppression of recombination of electron–hole pairs and effective separation of charge carriers. They have potential applications in water treatment, organic degradation, and photovoltaic devices. Due to the energy gradient existing at the interface electrons and holes are separated on the different sides of the heterojunctions [5, 6].

Nitrophenols are among the most harmful chemical byproducts of industries and are proved to cause methemoglobinemia, cyanosis, confusion, cancer, unconsciousness, etc. This can be converted into a non-toxic and industrially useful chemical intermediate viz 4-amino phenol by reduction. Methods like catalytic hydrogenation of 4-NP in ethanol under high temperature and pressure is tedious and involve the formation of aniline as byproduct. The hydrogenation of 4-NP using sodium borohydride and nano catalyst overcome the aforementioned problems and the conversion is carried out instantaneously under mild conditions [7–10].

Multidrug resistant microbes are severe threats to mankind and cause chronic diseases like typhoid, tuberculosis, pneumonia, etc. Recently mixed metal oxide nanocomposites have shown to be the ideal candidates as antibacterial agents. Small size, large surface area, lower toxicity, higher stability, desired morphology and defects in the crystal structure make them suitable for greater antibacterial performances [11].

Heterogeneous semiconductor coupling between n-type TiO_2 semiconductor and a p-type semiconductor $BiFeO_3$ has been reported to be an effective way to inhibit the charge carrier recombination and promote their separation [12]. Heterojunction creates an interface between hole-rich and electron-rich semiconductors. When electrons move to the p-type semiconductor and holes to the n-type, electronic equilibrium is attained. This electric dipole layer at the interface has positive charge region attracted towards n-type semiconductor and negative charge towards the p-type semiconductor. Thus, band bending occurs at p–n junction. The free flow of electrons to n-type semiconductor and the transport of holes to p-type semiconductors facilitate separation of charge carriers and improve the photocatalytic efficiency. The mixed metal oxide nanocomposites increase the life time of the photogenerated electrons and holes, creating more crystal defects with many oxygen vacancies and result in greater photocatalytic performance [13]. Also, noble metals such as Au and Ag have electron storage properties which promote charge separation in heterogeneous metal doped semiconductor systems [14].

Due to the unique characteristics like chemical stability, natural abundance, very high electrical conductivities and optical properties copper oxide nanoparticles find versatile applications [15]. The doping or coupling of CuO with transition metals reduces the band gap energy with red shift to the visible range. CuO is a p-type semiconductor with a narrow band gap of 1.2 eV. It can be doped with noble metal such as silver which provides the crystal defect to trap the electron, thereby enhancing the photocatalytic efficiency [16–19]. Coupling of CuO with metal oxides has been reported to have hostile effect against pathogenic bacteria and also silver doping increases antimicrobial activity. SnO_2 and ZnO are typical n-type semiconductors with wide band gap energies 3.59 eV and 3.32 eV, respectively [20, 21]. Nowadays, SnO_2 has become an important semiconductor metal oxide due to its potential applications in environmental remediation, photocatalysts, batteries, antibacterial agents and gas sensors [22]. Composites of ZnO with different metal oxides help to adjust their optoelectronic

and magnetic properties. The Schottky defects and oxygen vacancies in ZnO nanocrystals impart antibacterial activity [23].

In the present work, *Sida rhombifolia* functions as capping and complexing agent to synthesize Ag@ZnO/CuO (AZC) and Ag@SnO_2/CuO (ASC) heterostructured nanocomposites. It is a medicinal plant from the family of Malvaceae which contains the bioactive components like alkaloids, phytosteroids, glycosides, flavonoids, lignin, saponins and fixed oils [24].

In this study, ASC and AZC nanocomposites were prepared for the first time by one-pot green synthesis. *Sida rhombifolia* leaf extract was added to $Zn(NO_3)_2$ and $Cu(NO_3)_2$ solutions and calcined. Then, the CuO coupled ZnO/SnO_2 nanocomposites was decorated with Ag NPs. Besides, the photocatalytic performance of heterostructured nanocomposites was determined for the degradation of Methylene Blue (MB) and Methyl Orange (MO). The catalytic activity of the nanocomposites in the reduction of 4-NP using $NaBH_4$ has been investigated. The integrated binary nanocomposites exhibited hostile effect on the different five bacterial strains and were proved to be comparable with commercial antibiotics.

Experimental

Chemicals

Silver nitrate, stannic chloride, cupric nitrate, zinc nitrate, hydrogen peroxide, 4-nitro phenol, sodium borohydride, methyl orange and malachite green dye were purchased from Merck chemical reagent Co. Ltd. India. The *Sida rhombifolia*, a locally available weed was used for the preparation of plant extract. The bacterial strains used for screening were Gram negative *E. coli* (MTCC 2842), *P. aeroginosa* (ATCC 27,853), *K. pneumoniae* (ATCC 27,853) and Gram positive *S. aureus* (MTCC 3160) and *S. mutans* (MTCC 890). Stock solutions of MG and MO were prepared by dissolving 400 mg of dye in one liter of millipore water.

Characterization

X-ray diffraction technique was employed for studying the crystallinity and particle size using a Rigaku Miniflex-600: 40 kV and 20 mA current with Cu-Kα radiation ($\lambda = 0.1542$ nm) in the range from 2θ: 20°—80°. The surface morphology was determined using FESEM (FEI Nova NanoSem 450 electron microscope. Via Fluorescence spectrophotometer (Agilent, Cary Eclipse), the photoluminescence measurements were determined. UV–visible diffuse reflectance spectra were used to determine the band gap energies of biosynthesized nanocomposites (Jasco-v-550 UV/Visible spectrophotometer). By using a Netzsch-STA 449-F5 machine, thermogravimetric analysis (TGA) was monitored, in the temperature range 30–800 °C at heating rate 10 °C /min under N_2 environment. FT-IR spectra were used to determine the functional groups present in the nanocomposites (Agilent-Technologies-Cary 630—ATR). The UV–visible absorbance of MO, MG and hydrogenation of 4-nitrophenol solutions were recorded at regular intervals of time using a UV–visible spectrophotometer (Intech UV–Visible Spectrophotometer-Double beam-2800).

Biosynthesis of nanocomposites AZC and ASC

The leaves of *Sida rhombifolia* was boiled with water at 80 °C for 30 min filtered and cooled. This leaf extract was heated with 5 g of zinc nitrate/tin chloride at 60 °C and stirred magnetically. To this copper nitrate and silver nitrate were added under vigorous stirring for half an hour and concentrated to get solid precipitate. This was dried in hot air oven at 100 °C for 12 h and then powdered to fine mass. AZC sample was calcined at 400 °C for 3 h and ASC sample was calcined at 600 °C for 2 h in a muffle furnace.

Photodegradation studies

Photocatalytic performance of the as-prepared nanocomposites was investigated under UV irradiation of cationic and anionic dyes. Characteristically, 250 mg of catalyst was added to the dye solution (100 mL, 10 mg/L). To attain adsorption–desorption equilibrium, the solution was kept in dark for 30 min. 0.1 ml of H_2O_2 was added to the solution. It was subjected to irradiation in the photoreactor by a UV light source (150 W) and cooled by water circulation. At regular time intervals, aliquots were procured and centrifuged. The centrifugate was analyzed by UV–Vis spectrophotometer. The photodegradation efficacy of the catalysts was determined by following equation.

$$\text{Degradation efficiency } (\%) = \frac{C_0 - C_t}{C_0} \times 100 \quad (1)$$

where C_0 and C_t are the dye concentration initially and after time t, respectively.

Reduction of 4-nitrophenol

In a typical experiment, 5.0 mg catalyst was mixed with 250 mM (20 mL) 4-nitrophenol and freshly prepared $NaBH_4$ under magnetic stirring. 0.1 mL of the reaction mixture was withdrawn at regular time intervals. 5 mL of 2 M HCl was added to quench it. UV–Vis spectroscopy was used to follow the reduction reaction at a wavelength of 400 nm.

Antibacterial assay

The antimicrobial activity of the nanocomposites ASC and AZC was investigated for different bacterial strains by the well agar diffusion method. Gram-positive (*S. aureus and S. mutans*) and gram-negative (*E. coli, P. aeroginosa and K. pneumonia)* bacterial strains were used along with agar medium. The agar nutrient medium was sterilized at 130 °C for 40 min in an autoclave. It was transferred to the Muller Hinton agar plate and the bacterial lawn was cultured. Wells of approximately 7 mm was bored using a well cutter and 250 mg of nanocomposite was added and incubated at 37 °C for 24 h. The antibacterial activity was assayed by measuring the diameter of the inhibition zone formed around the well. Streptomycin was used as a positive control [25].

Results and discussion

XRD

The composition and crystal structure of the heterostructured nanocomposites were scrutinized by XRD. As shown in Fig. 1a, the XRD pattern of the pure SnO_2 sample exhibits strong diffraction peaks at 2θ values of 26.50° (110), 33.92° (101), 38.04° (200), 51.90° (211), 54.88° (220), 57.60° (002), 61.94° (310), 66.0° (202), and 68.28° (222) which match well with the corresponding peaks of the tetragonal structure of SnO_2, (JCPDS 01–077–0447). The CuO sample displays peaks at 2θ values of 32.16° (110), 35.66° (002), 38.08° (111), 46.26° (112), 48.48° (202), 58.26° (202), 66.10° (311) and 68.30° (220) which point towards the monoclinic crystal structure of CuO (JCPDS 048–1548). The XRD pattern of ZnO shows peaks at 2θ = 31.74° (100), 34.42° (002), 36.20° (101), 47.62° (102), 56.76° (110), 63.01° (103), 66.24° (200), 67.98° (112) and 69.02° (201), which coincide well with the characteristic peaks of hexagonal wurtzite structure (JCPDS 36–1451). The peaks at 2θ = 39.10°, 44.32° and 64.52° are ascribed to (111), (200) and (220) planes of metallic Ag [26]. The formation of a p-n heterojunction in heterostructured nanocomposites is indicated by the enhanced diffraction peaks [27].

The average crystallite size of AZC and ASC was found to be 36.36 and 35.09 nm, respectively, which is calculated using Scherrer's formula.

$$D = \frac{k\lambda}{\beta \cos\theta} \tag{2}$$

where D is the particle size in nm, λ is the wavelength of the radiation (1.541 A° for Cu Kα radiation), k is a constant equal to 0.9, β is the peak width at half-maximum intensity and θ is the peak position.

FTIR

Figure 1b displays the FT-IR spectrum of AZC and ASC nanocomposites. The broad band ranging from 3500 to 3000 cm^{-1} corresponds to the stretching vibrations of hydroxyl groups of the adsorbed water at surface of the catalyst while the peaks around 1630 and 1625 cm^{-1} are attributed to the bending vibrations [28]. The broad peak at 2340–2380 cm^{-1} may be due to the CO_2 present in the instrument [29]. The peaks between 1000–700 cm^{-1} and the other peak at 1380 cm^{-1} are related to the CO_3^{2-} vibrations [23]. The peaks below 1000 cm^{-1} confirm the presence of metal –oxygen bonds [30, 31].

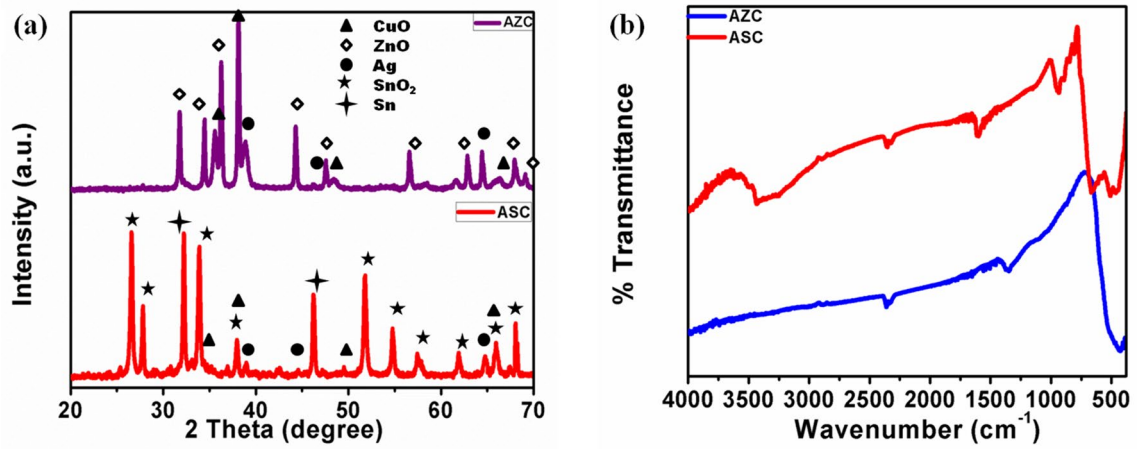

Fig. 1 **a** XRD patterns and **b** FTIR spectra of AZC and ASC

UV-DRS

The UV–visible diffuse reflectance spectra (DRS) of the photocatalysts are illustrated in Fig. 2a and b. The absorption curve for pure SnO_2 and ZnO as reported in the literature depict absorption in the UV region only [32, 33]. It can be observed that AZC shows enhanced absorption in the visible light region upto 900 nm, indicating the higher photocatalytic efficiency suggesting a synergistic effect of the heterojunction between ZnO and CuO. However, ASC exhibits absorption shift to the visible region slightly only compared to AZC. As CuO is a p-type semiconductor with narrow band gap, when combined with wide band gap metal oxides such as SnO_2/ZnO exhibit continuous light absorption in the sort of 400–800 nm with red shift due to development of p–n junction. The Tau plot from UV-DRS data help to determine band gap energy of the ASC and AZC nanocomposites. The tau plot equation is as shown below [34]:

$$(\alpha h\upsilon)^n = B\left(h\upsilon - E_g\right) \tag{3}$$

where α is the absorption coefficient, B is a constant related to the material, $h\nu$ is the photon energy in eV, h is Planck's constant, Eg is the optical bandgap in eV, n is an exponent that can take a value of either 2 for a direct transition or 1/2 for an indirect transition.

Inset of Fig. 2a and b, presents the tau plot and the straight-line portion of $(\alpha h\nu)^2$ versus energy ($h\nu$) on extrapolation gives the band gap energy. The bandgap value is obtained as 2.3 eV for Ag/SnO_2/CuO and 1.8 eV for Ag/ZnO/CuO, respectively. As shown in Fig. 2, the band gap energy of ASC is greater than that of AZC. The above results point towards the higher photocatalytic efficiency of AZC compared to ASC. Thus, the heterojunction of ZnO and CuO provides a more suitable band gap for the absorption of visible light [35]. In such heterostructured nanocomposites, new electronic states are created below the conduction band of the material which reduces the band gap energy.

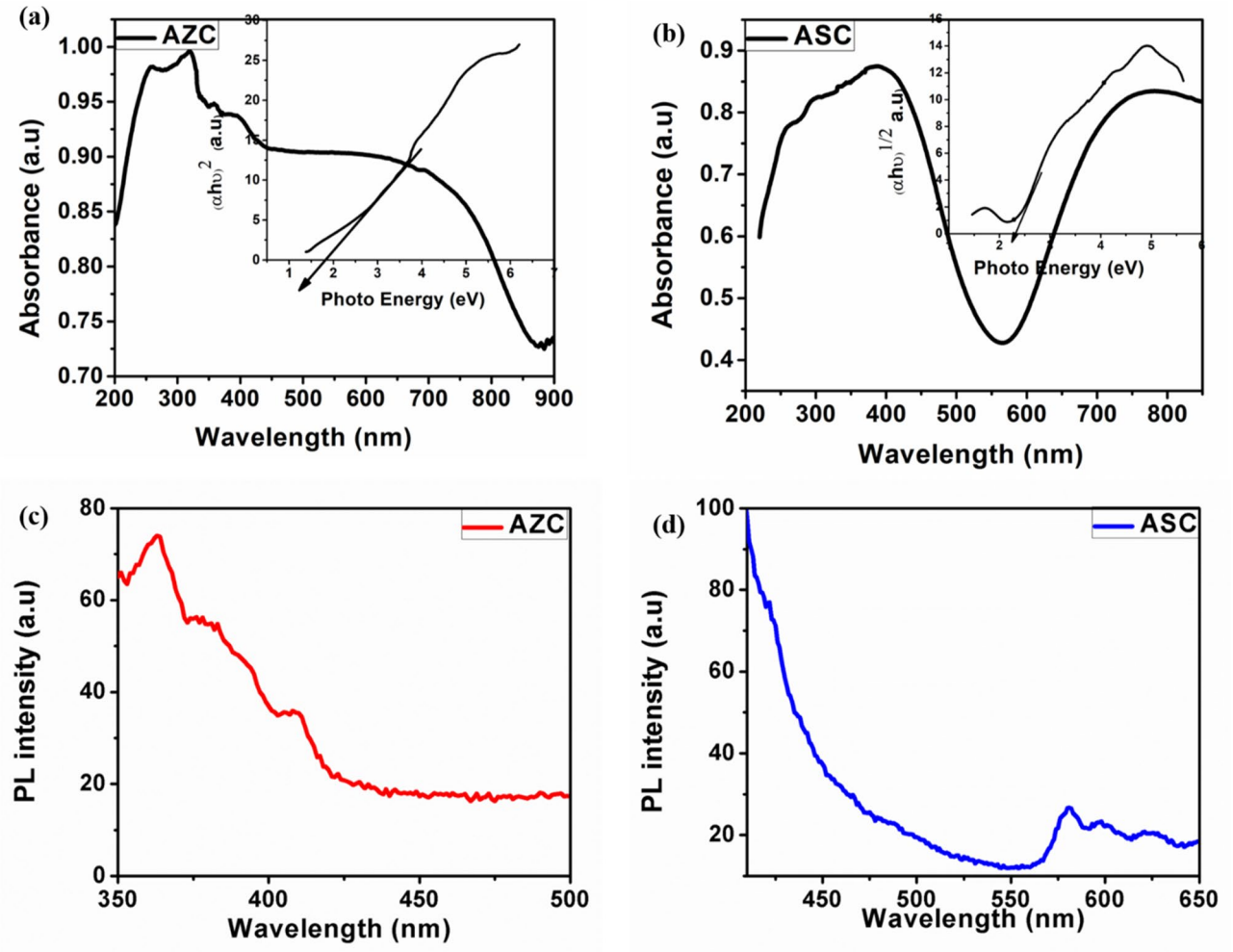

Fig. 2 UV–Visible DRS spectra (inset: Tauc plot) of **a** AZC; **b** ASC and PL spectra of **c** AZC; **d** ASC

Vijyalakshmi et al. reported the synthesis of Zn doped SnO_2 with decreased band gap value [36].

PL spectra

Photoluminescence spectra of AZC and ASC are shown in Fig. 2c and d, which was obtained with excitation wavelengths of 325 and 350 nm, respectively. In the case of AZC, ultraviolet emission called near-band-edge (NBE) emission is observed at 390 nm. Others are violet emission at 425 nm and blue emission at 460 nm. The perfect crystalline structures of the ZnO nanoparticles are responsible for NBE emission [36]. For ASC, the visible light emission (violet) at 425 nm reveals the defects of tin lattice or dangling bonds [37]. The photoluminescent peaks at 480 and 550 nm result from the oxygen vacancies and tin interstitials [38]. The observed broad PL peak in the range of 560–620 nm also indicates the crystal defects. The coupling of p-type CuO with n-type SnO_2/ZnO results in decreased PL intensity of heterostructured nanocomposites. This indicates that the formation of p-n heterojunction of SnO_2/ZnO and CuO which facilitate the separation of electron–hole pairs as the electron is transferred to CB of ZnO/SnO_2 from CB of CuO [39]. The lowering of rate of recombination of charge carriers enhances the photocatalytic efficiency.

FESEM

The detailed morphology of the heterostructured nanocomposites (AZC and ASC) was investigated by FESEM. Figure 3 shows the irregular aggregates of particle size between 100 and 500 nm for AZC whereas distorted spheres are arranged almost uniformly for ASC.

TGA

The thermal stability of the heterostructured nanocomposites was inspected by thermogravimetric analysis (Fig. 4). The physically adsorbed water gets removed from ASC at about 150 °C. The degradation is gradual and is pronounced at a temperature of 600 °C only. A weight loss of 24% is observed at 850 °C. AZC remains stable upto 800 °C and gives a char yield of 97% at 850 °C.

Reduction of 4-Nitro phenol

The catalytic activity of ASC and AZC nanocomposites was studied in the reduction of aqueous solutions of 4-NP in the presence of $NaBH_4$ at ambient temperature. When the as-prepared nanocomposites are added to the reaction system, the peak at 400 nm decreases and a new peak appears at about 268 nm, corresponding to 4-aminophenol hydrochloride, as shown in Fig. 5. Finally, the yellow color of the solution changes to white, showing the conversion of

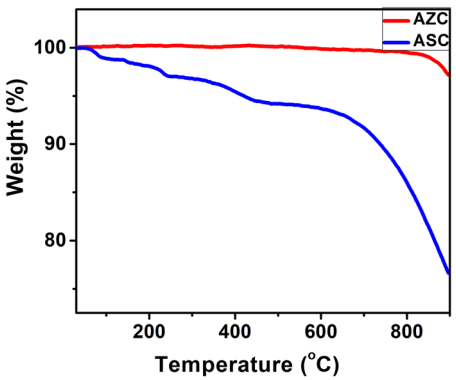

Fig. 4 TGA of biosynthesized AZC and ASC

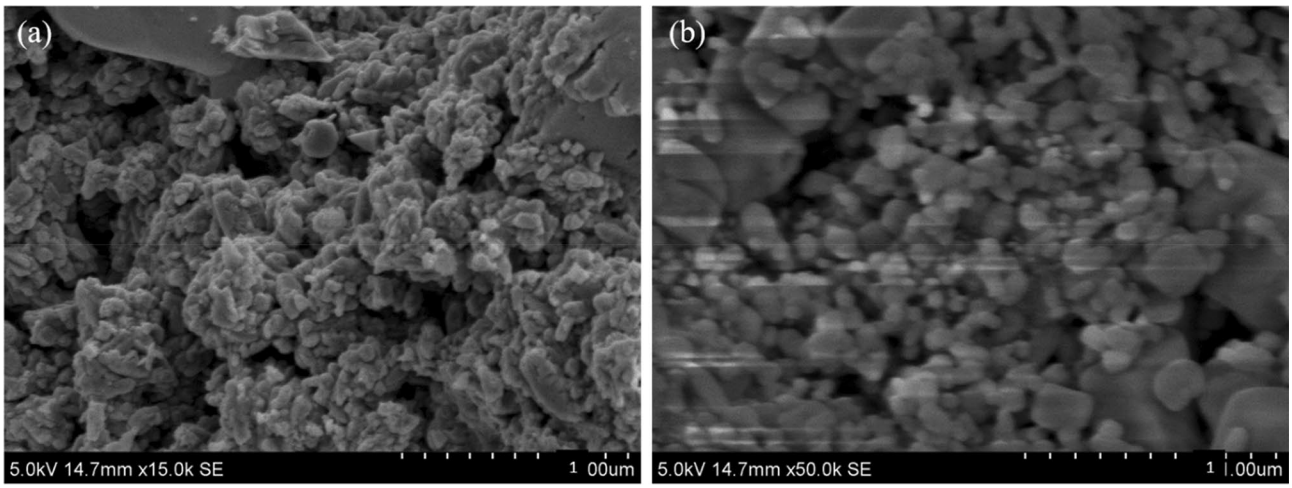

Fig. 3 FESEM micrographs of **a** AZC and **b** ASC

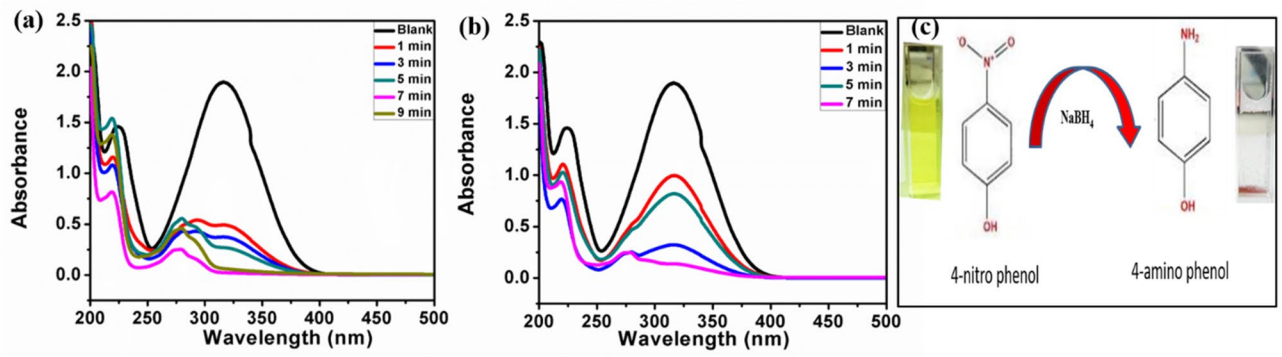

Fig. 5 Absorption spectra for the reduction of 4-NP to 4-AP by $NaBH_4$ in aqueous medium in the presence catalyst **a** AZC **b** ASC and **c** Colour change during catalytic reduction of 4-NP to 4-AP

4-NP to 4-AP. Reduction of 4-NP to 4-AP using $NaBH_4$ was investigated to study the catalytic activity of AZC and ASC. The whole peak at 400 nm disappears after 7 min and 9 min, respectively, for AZC and ASC, respectively. The results also show that pure NPs can catalyze 4-NP reduction to 4-AP, but with at slower reaction rates compared with heterostructured nanocomposites leading to a synergistic effect. ASC and AZC nanocomposites showed the best catalytic performance of all catalysts investigated. Compared to other catalysts like doped La_2O_3 which need 90 min to complete the reduction reaction but as-prepared catalysts showed the reduction reaction instantaneously [40].

Mechanism

4-NP in the presence of $NaBH_4$ undergoes deprotonation to nitrophenolate ions. Borohydride ions are adsorbed onto the surface of as-prepared nanocomposites and transfer electrons to the active Ag-shell present at the surface. ASC and AZC nanocomposites show greater catalytic activity and this might be due to the active Ag shell and positively-charged Ag-OH groups which are capable of adsorption of 4-nitrophenol molecules. The core metal oxide is capable of accumulating electronic charge onto it and act as electron acceptors. Thus, charge separation occurs between the metal oxide and silver particles. The flow of electrons from Ag particles ends up with an electron rich space at the interface of core. The 4-nitrophenolate ions get easily adsorbed onto the positively charged core particles. At the interface the reduction of 4-NPs into the 4-aminophenol occurs.

Photodegradation activity

Figure 6 shows the photocatalytic degradation efficiency of Ag doped SnO_2/ CuO and CuO/ZnO composites,

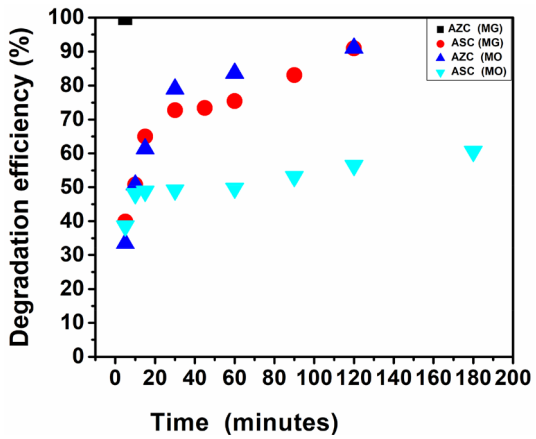

Fig. 6 Photodegradation efficiency Vs time plot of MG and MO for AZC and ASC

respectively, for MG and MO dyes under visible light irradiation using the Eq. (1). The absorption maxima of MG and MO were observed at 620 nm and 457 nm, respectively. In the case of $Ag@SnO_2$/CuO nanocomposites, the photodegradation was almost completed after 180 min for MG and MO. Ag@CuO/ZnO nanocomposites took only 5 and 120 min, respectively, for MG and MO for complete discolouration. The results reveal that compared to ASC composite, AZC sample degrades the dyes faster and easier with red shift to visible light. This can be explained with UV-DRS spectra as revealed from tau plot. The lower band gap energy for AZC (1.5 eV) impart greater photocatalytic efficiency than ASC (2.1 eV). The increase in photocatalytic efficiency can also be attributed to the formation of p–n type heterojunction. The free flow of electrons to n-type semiconductor and holes to p-type semiconductors favors separation of charge carriers and hence suppressing their recombination.

Mechanism of photocatalysis

CuO is considered to be an ideal visible light photocatalyst. It is p-type semiconductor with a narrow band gap energy of 1.35–1.79 eV [41]. But the indifferent potentials of the valence band (VB) and conduction band (CB), make it a less efficient photocatalyst [42]. When CuO is coupled with SnO_2/ZnO, the p-n heterojunction developed creates an interface between hole-rich and electron-rich semiconductors. The photo induced electrons on M will transfer to CuO (Fig. 7).

$$M + \mathrm{CuO} + h\upsilon \rightarrow \quad e^- + h^+ \tag{4}$$

The photo excited electrons from M transfer to the Ag NPs to equalize Fermi energy level. This results in the separation of photo induced electron hole pairs and the reduction reaction of the surface oxygen adsorbed on Ag NPs with electrons to $O_2^{\cdot -}$

$$\mathrm{Ag} + e^- \rightarrow \quad \mathrm{Ag}(e^-) \tag{5}$$

$$\mathrm{O_2} + \mathrm{Ag}(e^-) \longrightarrow \mathrm{O_2^{\bullet -}} \tag{6}$$

The photo induced electrons of n-type metal oxide semiconductor are transferred to the conduction band of Cu (II), which get reduced to Cu (I) which combines with oxygen to produce hydrogen peroxide and further produce hydroxyl radicals. They mineralize the organic pollutants.

$$\mathrm{Cu^{2+}} + e^- \rightarrow \mathrm{Cu^+} \tag{7}$$

$$2\mathrm{Cu^+} + \mathrm{O_2} + 2\mathrm{H^+} \longrightarrow 2\mathrm{Cu^{2+}} + \mathrm{H_2O_2} \tag{8}$$

$$\mathrm{OH} + \ \mathrm{dye} \longrightarrow \mathrm{CO_2} + \mathrm{H_2O} \tag{9}$$

Alternately electrons on the CB of metal oxide abstract oxygen to produce super oxide anion radical. This combines with water to give hydroxyl radicals. This can be represented as follows.

$$\mathrm{M}(e^-) + \mathrm{O_2} \longrightarrow \mathrm{M} + \mathrm{O_2^{-\bullet}} \tag{10}$$

$$\mathrm{O_2^-} + \mathrm{H_2O} \longrightarrow \mathrm{HO_2} \bullet + \mathrm{OH}\bullet \tag{11}$$

$$\mathrm{HO_2} \bullet + \mathrm{H_2O} \longrightarrow \mathrm{OH} \bullet + \mathrm{H_2O_2} \tag{12}$$

$$\mathrm{H_2O_2} \longrightarrow 2\mathrm{OH}\bullet \tag{13}$$

$$\mathrm{Dye} + \mathrm{OH} \bullet \longrightarrow \mathrm{Degradation\ Products} \tag{14}$$

Thus, heterostructured metal oxide nanocomposites of CuO with n-type semiconductors such as ZnO and SnO_2 show improved photocatalytic efficiency and extends the absorption to visible region.

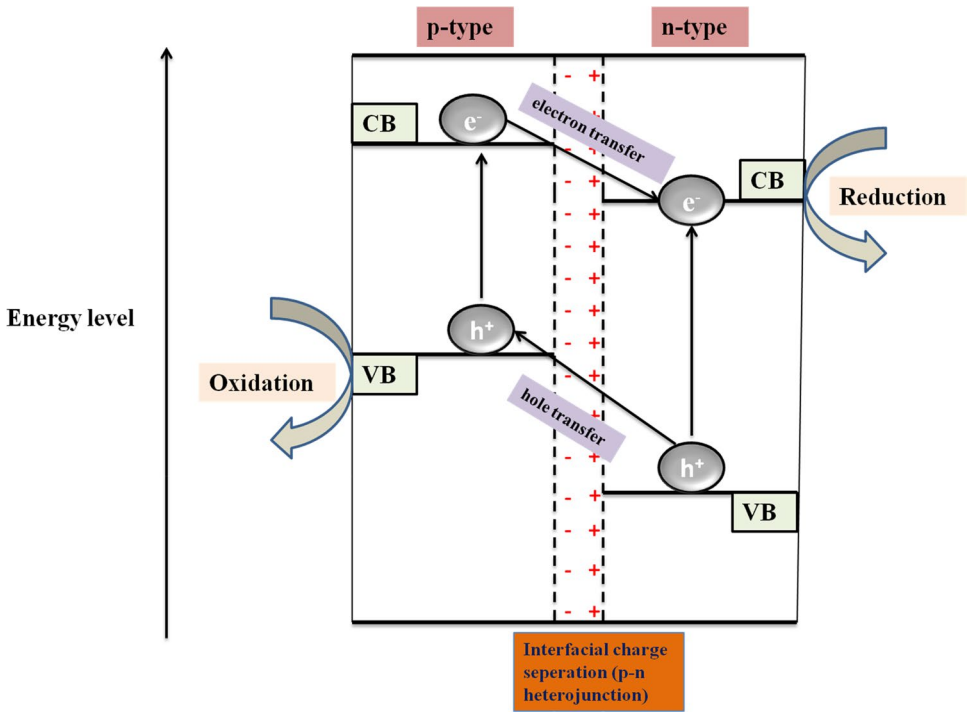

Fig. 7 Schematic diagram of the formation of a p – n junction and the possible charge-separation process

Antibacterial applications

The antibacterial activity of the heterostructured nanocomposites of silver doped CuO coupled ZnO/SnO_2 was investigated by agar well diffusion assay. Figure 8a–e shows the inhibition zones for different gram positive and gram-negative bacteria. It is interesting to note that ASC samples show much higher inhibition zone values than that for commercial antibiotic streptomycin Fig. 8f. The synergistic effect of silver and copper nanoparticles imparts superior antibactericidal property to the heterostructured nanocomposites both ASC and AZC.

Mechanism of antibacterial activity

Silver ions exhibit their antimicrobial activities by attaching to DNA molecules and -SH group of proteins which lead to denaturation of proteins. ROS like superoxide anions $\left(O_2^{\bullet-}\right)$ hydrogen peroxide (H_2O_2), and hydroxyl radicals ($OH^{\cdot}$) permeate through the cell membrane and damage the cell surface [43, 44]. AgNPs form complexes with the selected groups present in proteins and inactivate enzymes [45]. CuO NPs are known to exhibit excellent antibacterial properties. This is possibly by generating reactive oxygen species (ROS) which get attached to the cell membrane and disrupt the cell wall. It results in the decreased level of ATP and cause cell death [46, 47]. The heterostructured composites containing CuO NPs release $Cu.^{2+}$ ions which attack the negatively charged cell surface and hinder the activity of proteins [48, 49]. The large surface area of Ag@CuO/ZnO and Ag@CuO/SnO_2 nanocomposite affects the antibacterial activity. The release of metal ions and formation of reactive oxygen species inhibit the bacterial growth and kill them [50, 51]

Conclusion

The biogenic route for the synthesis of Ag@CuO/ZnO and Ag@ using the leaf extract of *Sida rhombifolia* has become an economically viable and environmentally sustainable method CuO/SnO_2 heterostructures. This green technique eliminates the consumption of toxic organic chemicals for the synthesis of multifunctional integrated nanometal oxides. As a p-type semiconductor with narrow band gap, CuO contribute much towards the enhancement of continuous light absorption of the heterostructured nanocomposites. The excellent photocatalytic performance of ASC and AZC for the degradation of both cationic (MG) and anionic (MO) dyes

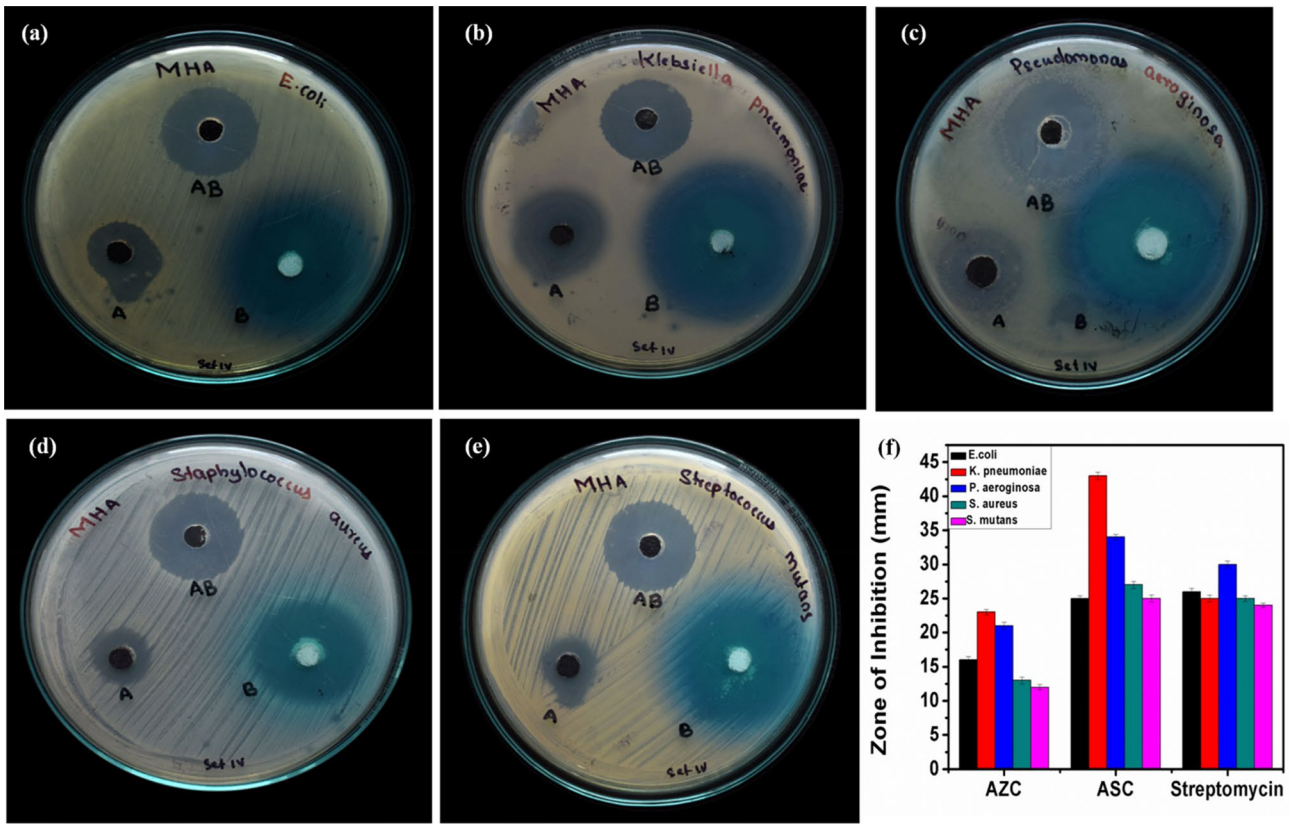

Fig. 8 Antimicrobial activity of biosynthesized AZC **(A),** AZC **(B)** and streptomycin **(AB)** against **a** *E. coli,* **b** *K. pneumonia,* **c** *P. aeroginosa,* **d** *S. aureus* and **e** *S. mutans* **f** Bar graph

might be due to developed p-n heterojunction at the interface. The hydrogenation reaction of 4-NP to 4-AP with these catalysts was found to be instantaneous. Due to the synergistic effects of heterostructures, ASC and AZC show antagonistic effect towards the growth of *Escherichia coli, Klebsiella pneumoniae, Pseudomonas aeroginosa, Streptococcus mutans and Staphylococcus aureus* with greater inhibition zones. Thus, the simple, low-cost and eco-friendly green method provides a revolutionary way of fabricating heterostructured silver doped nanocomposites of metal oxides having the potential as antibacterial and catalytic activities.

Acknowledgements The authors are thankful to Dr. Sujith, Associate professor, National Institute of Technology, Calicut, Kerala for supporting us to carry out the antibacterial work successfully. This research did not receive any specific grant from funding agencies in the public, commercial, or not-for-profit sectors.

References

1. J. Zhang, J.H. Bang, C. Tang, P.V. Kamat, ACS Nano **4**, 1 (2010)
2. G. Krithika, R. Saraswathy, M. Muralidhar, D. Thulasi, N. Lalitha, P. Kumararaja, A. Nagavel, R. Arun Balaji, R. Jayavel, J. Nanosci. Nanotechnol. **17**(8), 5209–5216 (2017). https://doi.org/10.1166/jnn.2017.13846
3. M. Hojamberdiev, G. Zhu, P. Sujaridworakun, S. Jinawath, P. Liu and J. P. Zhou, *Powder Technol.*, vol. 218, X (2012)
4. S.G. Ebbinghaus, H.P. Abicht, R. Dronskowski, T. Müller, A. Reller, A. Weidenkaff, Prog. Solid State Chem. **37**, 2–3 (2009)
5. K.R. Gopidas, M. Bohorquez, P.V. Kamat, J. Phys. Chem. **94**, 16 (1990)
6. Z. L. Liu, J. C. Deng, J. J. Deng and F. F. Li, *Mater. Sci. Eng. B Solid-State Mater. Adv. Technol.* 150, 99 (2008)
7. Y.T. Woo, D.Y. Lai, Patty's Toxicol. **2**, 104 (2012)
8. M. Nasrollahzadeh, M. Atarod, S.M. Sajadi, Appl. Surf. Sci. **364**, 636 (2016)
9. M. Nakagawa, D.G. Crosby, J. Agric. Food Chem. **22**, 5 (1974)
10. R. Dai, J. Chen, J. Lin, S. Xiao, S. Chen, Y. Deng, J. Hazard. Mater. **170**, 1 (2009)
11. K. Elumalai and S. Velmurugan, *Appl. Surf. Sci.*345 (2015)
12. Y. Liu, Chinese. J. Catal. **38**, 1052 (2017)
13. S. Vadivel, G. Rajarajan, J. Mater. Sci. Mater. Electron. **26**, 3155 (2015)
14. X. Yin, W. Que, D. Fei, F. Shen, Q. Guo, J. Alloys Compd. **524**, 13 (2012)
15. K. Mageshwari, R. Sathyamoorthy, J. Park, Powder Technol. **278**, 150 (2015)
16. Y.C. Zhang, L. Yao, G. Zhang, D.D. Dionysiou, J. Li, X. Du, Appl. Catal. B Environ. **144**, 730 (2014)
17. H. Wang, S. Kalytchuk, H. Yang, L. He, C. Hu, Y. Teohc and Andrey L. Rogach , *Nanoscale.* 6:11 (2014)
18. G. Lu, A. Linsebigler, J.T. Yates, J. Phys. Chem. **99**, 19 (1995)
19. Q. Gu, J. Long, H. Zhuang, C. Zhang, Y. Zhou, X. Wang, Phys. Chem. Chem. Phys. **16**, 24 (2014)
20. C. Wang, J. Zhao, W. Xinming, B. Mai, S. Guoying, P. Peng, J. Fu, Appl. Catal. B Environ. **39**, 3 (2002)
21. L. Zheng, Y. Zheng, C. Chen, Y. Zhan, X. Lin, Q. Zheng, K. Wei, J. Zhu, Inorg. Chem. **48**, 5 (2009)
22. P. Nazari, F. Ansari, B. AbdollahiNejand, V. Ahmadi, M. Payandeh, M. Salavati-Niasari, J. Phys. Chem. C **121**(40), 21935–21944 (2017). https://doi.org/10.1021/acs.jpcc.7b07061
23. R. Georgekutty, M.K. Seery, S.C. Pillai, J. Phys. Chem. C. **112**, 35 (2008)
24. A.T. Babu, R. Antony, J. Environ. Chem. Eng. **7**, 1 (2019)
25. A. Mangaiyarkarasi and M. H. M. Ilyas, *Int. J. Curr. Res. Biosci. Plant Biol.* 2015, 8 (2015)
26. J. Lu, H. Wang, S. Dong, F. Wang, Y. Dong, J. Alloys Compd. **617**, 869 (2014)
27. M.H. Sayadi, S. Ghollasimood, N. Ahmadpour, S. Homaeigohar, J. Photochem. Photobiol. A: Chem. **425**, 113662 (2022)
28. C. Mondal, J. Pal, M. Ganguly, A.K. Sinha, J. Jana, T. Pal, New J. Chem. **38**, 7 (2014)
29. Z. Miao, Y. Wu, X. Zhang, Z. Liu, B. Han, K. Ding, G. An, J. Mater. Chem. **17**, 18 (2007)
30. S.A. Khan, F. Noreen, S. Kanwal, A. Iqbal, G. Hussain, Mater. Sci. Eng. C. **82**, 46 (2018)
31. M. Hosseini-Sarvari, F. Moeini, New J. Chem. **38**, 2 (2014)
32. M.J. Chithra, M. Sathya, K. Pushpanathan, Acta Metall. Sin. **28**, 3 (2015)
33. S. Sarmah, A. Kumar, Indian. J. Phys. **84**, 1211 (2010)
34. E. Romanova, A. Melnikov, Y. Kuzutkina, V. Shiryaev, S. Guizard, A. Mouskeftaras, *Int* (Conf. Math. Methods Electromagn. Theory, MMET, 2012), pp. 521–526
35. N. Ahmadpour, M.H. Sayadi, S. Sobhani, M. Hajiani, J. Clean. Prod. **268**, 122023 (2020)
36. S. Vijayalakshmi, S. Venkataraj, M. Subramanian, R. Jayavel, J. Phys. D. Appl. Phys. **41**, 3 (2008)
37. G. Feng, W. Shu, L. Meng, C. Xiu, L. Su, Z.G. Dong, Y. Duo, J. Cryst. Growth **262**, 1–4 (2004)
38. E.J.H. Lee, C. Ribeiro, T.R. Giraldi, E. Longo, E.R. Leite, J.A. Varela, Appl. Phys. Lett. **84**, 10 (2004)
39. M.H. Sayadi, S. Homaeigohar, A. Rezaei, H. Shekari, Environ Sci Pollut Res. **28**, 15236 (2021)
40. T. Arai, M. Yanagida, Y. Konishi, Y. Iwasaki, H. Sugihara, K. Sayama, Catal. Commun. **9**, 6 (2008)
41. G. Ravi, M. Sarasija, D. Ayodhya, Nano Convergence. **6**, 12 (2019)
42. W. Shan, Y. Hu, M. Zheng, C. Wei, Dalt. Trans. **44**, 16 (2015)
43. L. Zhang, Y. Jiang, Y. Ding, N. Daskalakis, L. Jeuken, M. Povey, A.J.O. Neill, D.W. York, J. Nanoparticle Res. **12**, 5 (2010)
44. A. Sirelkhatim, S. Mahmud, A. Seeni, N.H.M. Kaus, L.C. Ann, S.K.M. Bakhori, H. Hasan, D. Mohamad, Nano-Micro Lett. **7**, 3 (2015)
45. M.H. Sayadi, N. Ahmadpour, S. Homaeigohar, Nanomaterials **11**, 2 (2021)
46. D. Das, B. Chandra, P. Phukon and S. Kumar, *Colloids Surfaces B Biointerfaces*, 101 (2013)
47. M. Abdollahi, M. Rezaei, G. Farzi, Int. J. Food Sci. Technol. **47**, 4 (2012)
48. D. Longano, N. Ditaranto, N. Cioffi, F. Di Niso, T. Sibillano, A. Ancona, A. Conte, M.A. Del Nobile, L. Sabbatini, L. Torsi, Anal. Bioanal. Chem. **403**, 4 (2012)
49. M. Raffi, S. Mehrwan, T.M. Bhatti, J.I. Akhter, A. Hameed, W. Yawar, M.M. Hasan, Ann. Microbiol. **60**, 1 (2010)
50. A. Azam, A. S. Ahmed, M. Oves, M. S. Khan and A. Memic, *Int. J. Nanomedicine*, 7 (2012)
51. J.A. Lemire, J.J. Harrison, R.J. Turner, Nat. Rev. Microbiol. **11**, 6 (2013)

Authors and Affiliations

Avis Tresa Babu[1] · Rosy Antony[2]

✉ Rosy Antony
drrosy.antony3@gmail.com

[1] Post Graduate and Research Department of Chemistry, Nirmalagiri College, Kannur, Kerala 670701, India

[2] Post Graduate Department of Chemistry, ITM College, Mayyil, Kannur, Kerala, India